Science of the Total Environment 858 (2023) 159940

Contents lists available at ScienceDirect

Science of the Total Environment

journal homepage: www.elsevier.com/locate/scitotenv

Biochar–goethite composites inhibited/enhanced degradation of triphenyl phosphate by activating persulfate: Insights on the mechanism

Yunjiang Yu [a], Zijuan Zhong [a,c], Haobo Guo [a], Yingxin Yu [c], Tong Zheng [a], Hongyan Li [a], Zhaofeng Chang [a,b,*]

[a] *State Environmental Protection Key Laboratory of Environmental Pollution Health Risk Assessment, South China Institute of Environmental Sciences, Ministry of Ecology and Environment, Guangzhou 510655, China*
[b] *Faculty of Environmental Science & Engineering, Kunming University of Science & Technology, Yunnan Provincial Key Laboratory of Soil Carbon Sequestration and Pollution Control, Kunming 650500, China*
[c] *Guangdong–Hong Kong–Macao Joint Laboratory for Contaminants Exposure and Health, Guangdong Key Laboratory of Environmental Catalysis and Health Risk Control, Institute of Environmental Health and Pollution Control, Guangdong University of Technology, Guangzhou, 510006, China*

HIGHLIGHTS

- TPhP can be effectively degraded in PDS alone system.
- Both BC35@FH and MBC80@FH facilitated PDS activation to produce more ROS.
- While BC35@FH inhibited TPhP degradation, MBC80@FH promoted TPhP degradation.
- $^1O_2$, $SO_4{\cdot}^-$ played a stronger degradation role than ·OH, $O_2{\cdot}^-$ in TPhP degradation.
- Hydroxylation, phosphorus oxygen and phenoxy bond breakage involved in degradation.

GRAPHICAL ABSTRACT

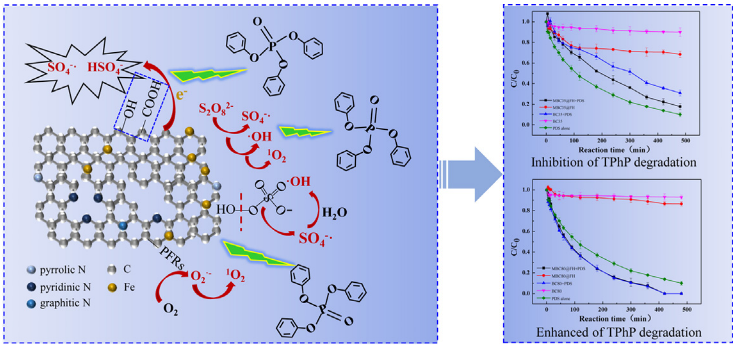

ARTICLE INFO

Editor: Baoliang Chen

Keywords:
Organophosphates
MBC@FH
Reactive oxygen species
Catalytic degradation
Activating mechanism

ABSTRACT

In this study, the biochar–goethite composites (MBC@FH) were synthesized through co–ball milling and the degradation of triphenyl phosphate (TPhP) was compared in persulfate (PDS) alone system and MBC@FH&PDS systems. The results showed that TPhP can be effectively degraded in PDS alone system and degradation efficiency reached up to 90 % within reaction of 8 h, at a PDS concentration of 10 mM, a reaction temperature of 30 °C and a system pH of 6.12. The obvious degradation can be ascribed to the reactive oxygen species (ROS) generated by self–decompose of PDS, among which $^1O_2$, ·OH and $O_2{\cdot}^-$ play a major role in the degradation process. Although 350 °C biochar–goethite composites (MBC35@FH) and 800 °C biochar–goethite composites (MBC80@FH) facilitated PDS activation to produce more ROS, the catalytic degradation of TPhP was different in their systems. The degradation of TPhP was inhibited by MBC35@FH due to its stronger adsorption for TPhP, while MBC80@FH promoted TPhP degradation and degradation efficiency was up to 100 % within 6 h. $^1O_2$ and $SO_4{\cdot}^-$ played a stronger degradation role than ·OH and $O_2{\cdot}^-$ in above systems. The transformation of Fe species, functional groups (oxygen–containing functional groups, pyrrolic nitrogen) and persistent free radicals (PFRs) on the MBC@FH were involved in the PDS activation to produce ROS. Furthermore, MBC80@FH was more capable of activating PDS than MBC35@FH due to its abundant defect sites, larger specific surface area, more PFRs, higher Fe content and stronger electron transfer capability. In addition, seven possible TPhP intermediates were identified and possible degradation pathways of TPhP were proposed accordingly. This study illustrated that not all metallic carbon catalysts are necessarily beneficial for organic contaminants degradation.

---

[*] Corresponding author at: State Environmental Protection Key Laboratory of Environmental Pollution Health Risk Assessment, South China Institute of Environmental Sciences, Ministry of Ecology and Environment, Guangzhou 510655, China.
E-mail address: changzhaofeng545@163.com (Z. Chang).

http://dx.doi.org/10.1016/j.scitotenv.2022.159940
Received 20 September 2022; Received in revised form 30 October 2022; Accepted 31 October 2022

1. Introduction

According to the Stockholm Convention, polybrominated diphenyl ethers (PDEDs) are classified as persistent organic pollutants (POPs) due to their environmental persistence and their hazard to human health (Cequier et al., 2014). The production and application of its substitute, organophosphates (OPEs) are increasing year by year. Thus, the environmental impact of OPEs has attracted extensive attention (Zhou et al., 2022). Triphenyl phosphate (TPhP) is a typical type of OPEs and is widely used as a flame retardant in textiles, cable insulation, and lacquers (Van der Veen and De Boer, 2012; Zhang et al., 2019). It is reported that TPhP production reached 14,493 tons in 2020, mainly for the production of foam seating, bedding, plastic rubber and polish products (Blum et al., 2019). As an additive, TPhP does not form chemical bonds with polymer material, resulting in its easy release into the environment during use and disposal. For example, the high concentration of TPhP were detected in sediments (Pearl River Delta, South China), wastewaters (Solekilen Wastewater Treatment Plant) and soils (e–waste recycling area, Northern Vietnam), which reached 656.7 mg/kg, 14,000 ng/L and 3300 ng/g, respectively (Zeng et al., 2014; Matsukami et al., 2015; Wang et al., 2018). In recent years, it has even been detected in a variety of living organisms, including human breast milk and urine, fish, and etc. (Kim et al., 2014; Zhao et al., 2019). In addition, studies have shown that TPhP is neurotoxic and reproductive toxic in organisms, posing a potential risk to human health (Canbaz et al., 2017; Hu et al., 2017). Therefore, there is an urgent need to develop an environmentally friendly method to remove TPhP from the environment.

In recent years, advanced oxidation processes (AOPs) have been widely used in the removal of contaminants based on the generation of reactive radicals, such as sulfate radicals ($SO_4{\cdot}^-$) and hydroxyl radicals (·OH) (Kong et al., 2022; Zhu et al., 2023). Compared with ·OH ($E^0 = 1.8–2.7$ V), $SO_4{\cdot}^-$ has higher redox potential ($E^0 = 2.5–3.1$ V), longer half–life, and wider pH adaptation range (Yang et al., 2017). In general, $SO_4{\cdot}^-$ can be produced by activating persulfate (PDS, $S_2O_8^{2-}$) through heat, ultrasound, and microwave (Zhu et al., 2019). Comparing with this, using transition metal cations or metal oxides to activate PDS can avoid the introduction of external energy, and the operation is simpler. For example, goethite (α–FeO(OH)), a mineral widely existing in environmental matrixes, has the characteristics of thermodynamic stability, environmental friendliness, and low cost (Zhang et al., 2020). It was often used as an iron source to activate PDS and generate $SO_4{\cdot}^-$. However, activation of PDS by α–FeO(OH) alone was not efficient in removing organic contaminants because of its aggregation tendency (Ge et al., 2017). To solve this problem, loading it onto carrier materials to avoid its aggregation is a feasible solution. Among the various supporting/stabilizing materials, biochar is considered feasible due to its economy and accessibility (Wang and Wang, 2019).

Biochar is an excellent carrier material, which has the advantages of low cost, environmental friendliness and stable structure (Dai et al., 2019; Lu et al., 2020; Shi et al., 2022). However, the limited porous structure and active sites of pristine biochar limit its application. Fortunately, biochar loading iron oxides such as Fe_2O_3, Fe_3O_4 could increase the defects sites, specific surface areas (SSA) of the composites and thus enhance the ability to catalyze PDS for contaminants degradation (Huang et al., 2021; Yu et al., 2022). Generally, biochar–mineral composites can be prepared by chemical precipitation, wet impregnation and carbothermic reduction (Zheng et al., 2020), but the high energy consumption, cumbersome operation and external pollution limited the development of these methods. Co–ball milling of inorganic minerals and biochar is an efficient, green, solvent free method (Shan et al., 2016). The biochar–mineral composites preparation by co–ball milling not only prevented goethite buildup, but also increased the SSA and functional groups of the composites, thereby enhancing its ability in the degradation of organic contaminants (Zhao et al., 2022). However, the catalytic performance of biochar–mineral composites often depends on the biochar properties. Fu et al. (2019b) found that biochar–Fe_3O_4 composites prepared at high temperature had higher graphitization degree and mesopores ration than those prepared at low temperature, thus exhibiting excellent peroxymonosulfate activation effect for p–hydroxybenzoic acid degradation. Mineral loading on 800 °C biochar also exhibited better degradation efficiency for bisphenol A than loaded on 350 °C biochar (Yu et al., 2022). To the best of our knowledge, no study has been conducted to investigate the TPhP degradation by biochar–mineral composites activating PDS and the effect of biochar properties on its catalytic degradation efficiency is not clear.

Considering the high TPhP concentration in wastewater from sewage treatment plants, it may become the source of TPhP in other environmental media. Thus, it is necessary to completely eliminate TPhP in wastewater. In this study, nitrogen–rich chicken feather was used as raw material to prepare biochar at different temperatures, and biochar–goethite composites were prepared by co–ball milling. The high nitrogen element could modulate the electronic properties of the sp2 hybrid carbon skeleton and generate more active sites on biochar materials (Liu et al., 2018), which may be beneficial for TPhP removal. The physicochemical properties of pristine biochar and its composites were characterized by Fourier transform infrared spectroscopy (FTIR), X–ray photoelectron spectroscopy (XPS), X–ray diffraction (XRD), etc. Biochar and the composites were used to degrade TPhP in the PDS system by conducting a series of kinetic experiments. The effects of reaction conditions, humic acid (HA), anions, and cations on the TPhP degradation were investigated. The purpose of this study was to (1) investigate the degradation efficiency and mechanism of TPhP in biochar–goethite & PDS systems; (2) compare the effects of different composites on catalytic degradation of TPhP and analyze the reasons; and (3) propose the possible degradation pathways of TPhP.

2. Materials and methods

2.1. Materials

Triphenyl phosphate (TPhP, 98 %), sodium chloride (NaCl), calcium chloride ($CaCl_2$), magnesium chloride ($MgCl_2$), iron chloride ($FeCl_3$), sodium bicarbonate ($NaHCO_3$), sodium dihydrogen phosphate (NaH_2PO_4), and potassium persulfate ($K_2S_2O_8$, PDS) were purchased from Aladdin (Shanghai, China). Goethite (α–FeO(OH), 30–63 % Fe), 5,5–dimethyl–1–pyrroline–N–oxide (DMPO, 97 %), 2,2,6,6–tetramethyl–4–piperidinol (TEMP, 98 %), methanol (MeOH), and *tert*–butanol (TBA, 99 %) were obtained from Sigma–Aldrich (Shanghai, China). p–benzoquinone (BQ, 98 %), L–histidine (99 %), and HA were received from Macklin Biochemical Co. Ltd., China. Ultra–pure water (≥18.25 MΩ·cm) was prepared using a water purification system (Ewell Bio, Guangzhou, China).

2.2. Preparation of catalysts

Chicken feathers were collected from a local market in Guangzhou. It was washed several times with deionized water and then dried at 60 °C for 48 h in an oven. The preprocessed chicken feathers were pyrolyzed in a tubular furnace (ZSK 1700, Cinite) at 350 and 800 °C for 4 h under N_2 atmosphere, with the heating rate of 10 °C/min, N_2 flow rate of 0.2 L/min. The prepared biochar was all crushed and sieved into the particle size to be <250 μm. Depending on the pyrolysis temperature, the obtained materials were named as BC35 and BC80.

Biochar–α–FeO(OH) composites were prepared in a planetary ball milling machine (F—P400, FOCUCY). The biochar and α–FeO(OH) were first mixed at a mass ratio of 1:2, and they were put in an agate tank (mass ratio of α–FeO(OH)/biochar composites to ball =1:100). Then, the ball milling was operated at 500 rpm for 12 h. During ball milling, the rotation direction was altered every 2 h. The obtained biochar–α–FeO(OH) composites were marked as MBC35@FH and MBC80@FH, which were stored in vials for subsequent tests.

2.3. Batch experiments

All the batch experiments were conducted in 40 mL brown glass test vials in a thermostatic water bath shaking instrument at 30.0 ± 0.2 °C.

The mixed reaction solution (20 mL) containing 10 μM of TPhP and 0.1 g/L catalysts without any pH adjustment (pH = 6.16). After adding 10 mM PDS to the solution, the reaction began. At fixed time intervals, 0.5 mL sample was withdrawn and immediately quenched by 0.5 mL pure methanol and filtered through a 0.22 μm membrane for TPhP analysis.

Besides, the optimal reaction conditions, such as catalyst dosage, PDS concentration, and pH in degradation process were previously evaluated. What's more, the sewage treatment plant influent and the effects of typical natural water components, including inorganic anions (Cl^-, HCO_3^-, and $H_2PO_4^-$), cations (Na^+, Ca^{2+}, Mg^{2+}, and Fe^{3+}) and representative dissolved organic matter HA on TPhP degradation were investigated. In addition, the toxicity and iron leaching content (Fe^{2+} ad Fe^{3+}) were measured to evaluated the ecological security of catalyst (Text S1 and S2). In order to explore the degradation mechanism, the reactive oxygen species (ROS) quenching and trapping experiments were conducted. ROS were scavenged with methanol (MeOH), *tert*–butanol (TBA), p–benzoquinone (BQ), L–histidine and trapped by 5,5–dimethylpyrroline–oxide (DMPO) and 2,2,6,6–tetramethyl–4–piperidinol (TEMP). The detailed measurement methods were described in Text S3.

2.4. Characterization and analytical methods

The residual concentration of TPhP in the system was determined by high–performance liquid chromatography (HPLC, Agilent 1200, Agilent Technologies) equipped with a UV detector. The mobile phase was 20:80 (V:V) of deionized water and acetonitrile, the flow rate was 1 mL/min and the wavelength for UV–vis spectrophotometer was 210 nm. Degraded intermediates of TPhP were detected by liquid chromatography system coupled to a tandem mass spectrometer (LC–MS/MS, AB SCIEX API4000, America) (Text S4). Heavy metal (Fe) concentration was determined by inductively coupled plasma and mass spectrometry (ICP–MS, NexION 2000, PerkinElmer).

The functional groups of catalysts were characterized by FTIR (Nicolet iS50, Thermo) and Boehm method (Boehm, 1994). The surface morphology and crystal structure of the catalysts were measured by scanning electron microscopy (SEM, S–4800, Hitachi) and XRD (martLab 3KW, Rigaku), respectively. Surface elemental compositions and chemical states of the catalysts were analyzed by XPS (Escalab 250Xi, Thermo). Biochar carbon structures were distinguished using Raman spectroscopy (Thermo Fischer DXR). Pore structure and SSA were measured by N_2 adsorption–desorption, using the Brunner – Emmett – Teller method (BET, AutoChem II 2920, Micromeritics). Electrochemical workstation (Huachen, CHI660) was used to analyze the electrochemical properties of the catalysts. In addition, the ROS in the reaction solution was detected by electron paramagnetic resonance spectroscopy (EPR, Bruker A300–10/12, Bruker). The detailed measurement parameters could be found in Text S5.

3. Results and discussion

3.1. Characteristic of catalysts

As shown in XRD pattern (Fig. 1a), BC35/80 showed a distinct diffraction peak around 23°, which assigned to the (002) plane of graphitic carbon (Yu et al., 2022), and the stronger peak intensity of BC80 than that of BC35, indicated a higher degree of graphitization/carbon crystallinity. After modification by α–FeO(OH), the diffraction peak of the graphitized structure reduced (Fig. 1a). The composite materials of MBC35/80@FH exhibited diffraction peaks at 17.8°, 21.2°, 26.3°, 33.2°, 36.7°, 53.2°, 58.9° and 63.9°, which can be ascribed to the (020), (110), (120), (130), (111), (221), (151) and (061) planes of α–FeO(OH) (JCPDS No. 29–0713),

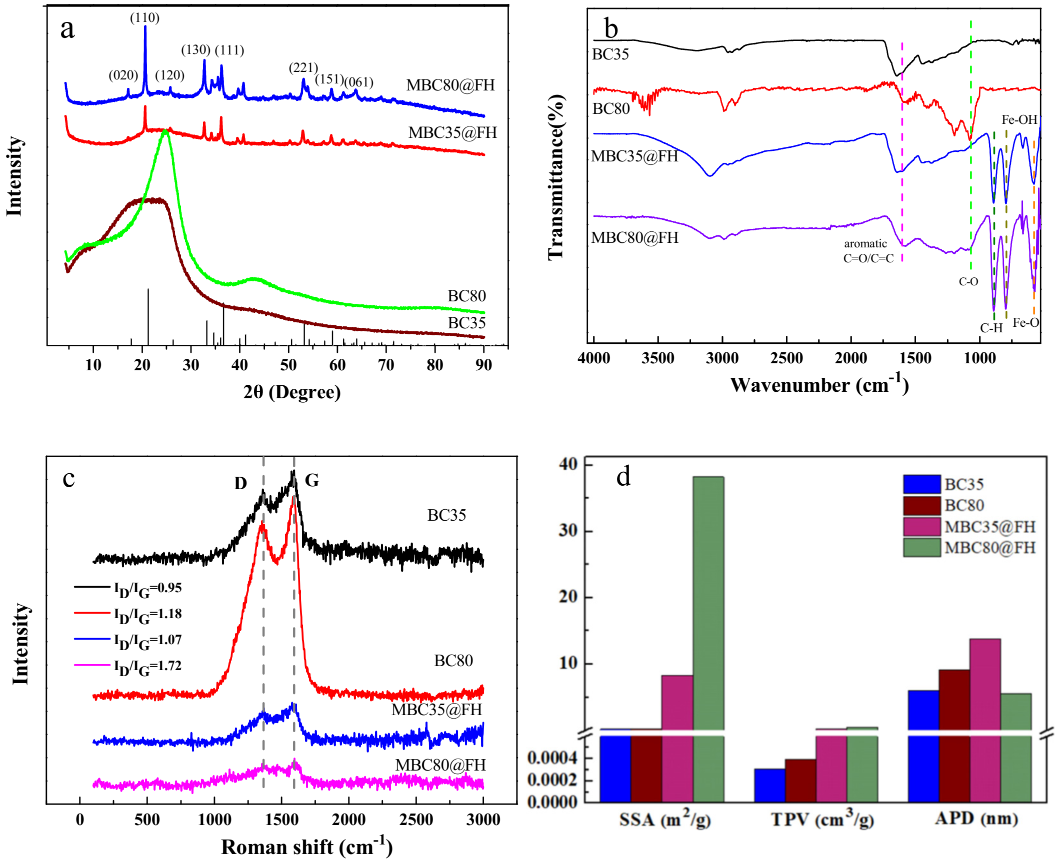

Fig. 1. XRD spectra (a), FTIR spectra (b), Raman spectra (c), SSA, TPV, and APD (d) for BC35/80, MBC35/80@FH. TPV: total pore volume; APD: average pore diameter; SSA: specific surface areas.

Table 1
The surface elemental composition and deconvolution of the C1s region bonding site.

Catalyts	$C1_S$ %	$N1_S$ %	$O1_S$ %	Fe2p %	C1 C–C/C = C	C2 C–O	C3 C = O	C4 O–C = O	Sum
BC35	76.63	12.25	10.86	0.13	0.48	0.30	0.09	0.13	0.52
BC80	80.91	10.09	8.66	0.17	0.81	0.01	0.10	0.09	0.20
MBC35@FH	67.71	11.24	18.25	2.56	0.36	0.27	0.21	0.15	0.63
MBC80@FH	61.72	9.22	22.74	6	0.46	0.24	0.12	0.18	0.54

respectively. XPS analysis showed that BC35 contained more oxygen–containing functional groups than BC80 (Table 1), and α–FeO(OH) modification increased the O and Fe content of MBC35/80@FH. All these results verified that α–FeO(OH) was successfully loaded on the biochar. The deconvolution results of C1s region bonding site indicated that loading α–FeO(OH) increased the content of oxygen–containing functional groups, such as C═O and O–C = O on the surface of composite biochar materials (Table 1). These increased oxygen–containing functional groups may be partly newly formed during ball milling and partly derived from α–FeO (OH). The O1s peaks of BC35/80 at 531.2–531.6 eV, 532.5–532.9 eV, 533.0–533.4 eV, and 534.8–535.2 eV were assigned to C═O, lipid C—O, aromatic C—O, and O_2/H_2O, respectively (Smith et al., 2016) (Fig. S1a and S1c). After loading α–FeO(OH), Fe—O and C–O–Fe/–OH replaced C═O and C—O (Yang et al., 2018) (Fig. S1). The appearance of C–O–Fe/–OH indicated that chemical bonds were formed between biochar and α–FeO(OH), suggesting that α–FeO(OH) was not simply covered on the surface of biochar, but existed in the form of bonded complexes. The FTIR results also showed that Fe—O (642 cm^{-1}) and Fe–OH (782 cm^{-1}) (Zhang et al., 2021) appeared on MBC35/80@FH (Fig. 1b), which was consistent with the XPS analysis results. In addition, the higher Fe content (6 %) of MBC80@FH than that of MBC35@FH (2.56 %) resulted in significantly stronger Fe—O and Fe–OH peaks intensities in the FTIR for MBC80@FH than for MBC35@FH (Table 1, Fig. 1b).

The Raman spectrum of all biochar materials showed obvious D (1340 cm^{-1}) and G (1580 cm^{-1}) bands (Fig. 1c). D band represents the amorphous carbon structure, whereas G band represents the graphitized carbon structure (Lin et al., 2019), and I_D/I_G value is often used to evaluate the degree of graphitization or defects in carbon materials (Ouyang et al., 2019). The I_D/I_G increased from 0.95 for BC35 to 1.18 for BC80 (Fig. 1c), indicating that the defect sites of pristine biochar increased with the increase of biochar preparation temperature. After loading α–FeO(OH), the I_D/I_G increased further, which may be due to forming the disordered structure of the composites. The I_D/I_G of BC80 and MBC80@FH was significantly higher than that of BC35 and MBC35@FH (Fig. 1c), indicating that 800 °C biochar materials can provide more catalytic active sites for pollutant degradation. SEM showed that BC35 and BC80 had obvious carbon skeleton structures with flat surfaces, but with fewer pores (Fig. 2a and d), which contributed to the small specific surface areas (Figs. 1d and S2). After loading α–FeO(OH), the carbon structure of MBC35/80@FH was broken and the surface became rough, and α–FeO(OH) was uniformly distributed on the surface of biochar (Fig. 2b and e). The rough surface can provide more reactive sites for PDS activation. In addition, the SSA and total pore volume (PTV) increased after loading α–FeO(OH) (Figs. 1d and S2), this may facilitate the mass transfer between the contaminant, oxidant, and catalyst. Energy–dispersive X–ray analysis (EDX) showed the surface Fe content of MBC80@FH (65 %) was higher than that of MBC35@FH (61 %), which was consistent with the results of XPS analysis. ICP–MS results further demonstrated that Fe content of MBC80@FH reached up to 401.28 μg/mg which was 1.63 times higher than that of MBC35@FH (245.51 μg/mg). Compared with MBC35@FH, the abundant defect sites, large SSA, TPV and high Fe content of MBC80@FH are favorable for its catalytic PDS generation of ROS to degrade organic contaminants.

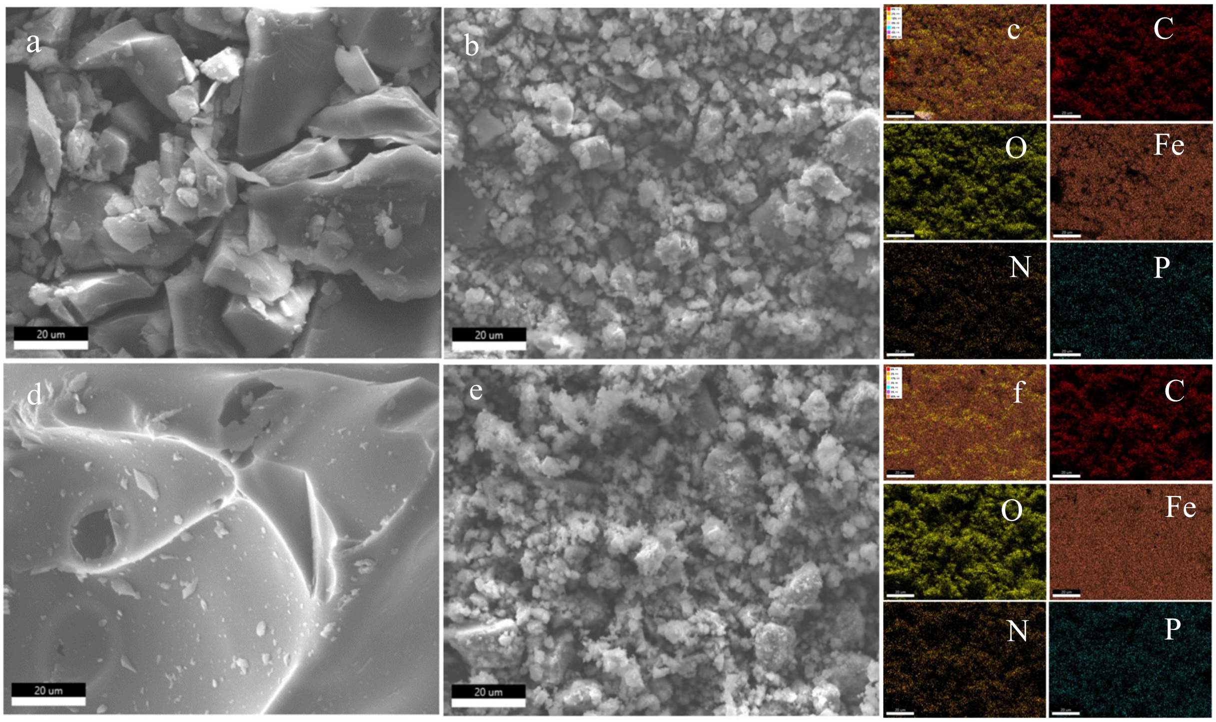

Fig. 2. The SEM spectra of BC35 (a), MBC35@FH (b), BC80 (d), MBC80@FH (e) and EDX–element distribution on biochar of MBC35@FH (c), MBC80@FH (f).

3.2. TPhP degradation in PDS alone and catalyst systems

PDS alone was found to be effective in degrading TPhP, with 90.0 % of TPhP was degraded after reaction 8 h at a PDS concentration of 10 mM, a reaction temperature of 30 °C and a system pH of 6.12 (Fig. 3). Other studies also reported that polychlorinated biphenyls (Fang et al., 2013) and antibiotics (Song et al., 2017) can be effectively degraded in the liquid phase when PDS existed alone. The researchers found that PDS can self–

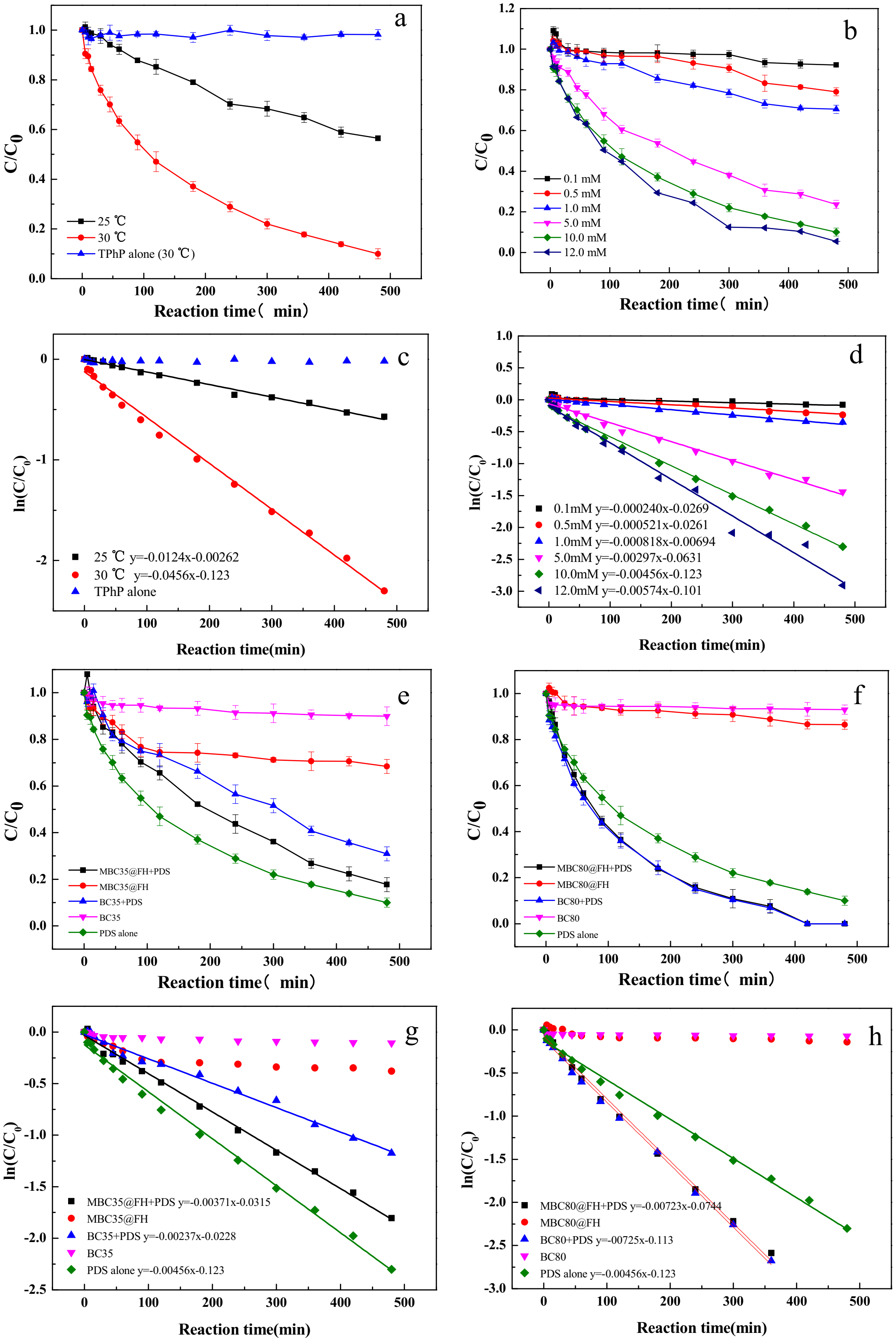

Fig. 3. The effect of reaction temperature (a, c), PDS concentration (b, d) on TPhP degradation in PDS alone system and degradation kinetics (e, f) of TPhP in MBC35/80@FH&PDS system. a, b, e, f: the degradation kinetics; c, d, g, h: pseudo–first–order kinetics fitting results. e, g: MBC35@FH&PDS; f, h: MBC80@FH&PDS. [TPhP] = 10 μM; [catalytic] = 0.1 g/L; [PDS] = 10 mM; [pH] = 6.12; [temperature] = 30 °C (e–h).

decompose to generate $SO_4\cdot^-$ (Eq. (1)) (House, 1962) at a certain temperature, $SO_4\cdot^-$ reacts with H_2O to generate ·OH, and then a series of reactions to generate ROS occurred (Eqs. (2)–(5)). The decomposition rate of PDS varies with the reaction temperature. At 25 °C, 40 °C and 50 °C, the decomposition rate is about 6.12×10^{-6} min^{-1}, 3.3×10^{-5} min^{-1}, 5.7×10^{-5} min^{-1}, respectively (House, 1962). In this case, the degradation efficiency and the pseudo–first–order kinetic reaction rate (k_{obs}) of TPhP increased with increasing of reaction temperature probably due to the fast decomposition rate of PDS at high temperature and produce more ROS (Fig. 3a and c). Similarly, the degradation efficiency and k_{obs} of TPhP increased with the concentration of PDS, which was due to the fact that higher concentrations of PDS could generate more ROS (Fig. 3b and d).

Pre–experiments revealed that TPhP obtained the best degradation effect in the catalytic degradation system with catalyst was 0.1 g /L, PDS was 10 mM and pH was 6.12 (Fig. S3). Under this condition, the catalytic degradation effect of different catalysts on TPhP were compared. As shown in Fig. 3e and f, BC35 and BC80 had a weak adsorption capacity for TPhP, and the adsorption removal rate was <10 %. Loading α–FeO(OH) increased the adsorption capacity of MBC35@FH and MBC80@FH for TPhP, with adsorption removal rates of 31.58 % and 13.51 %, respectively. MBC35@FH had a stronger adsorption capacity than MBC80@FH, probably because the partition mechanism played a major role in adsorption of hydrophobic organic contaminants (Guo et al., 2020; Wu et al., 2022). After adding PDS to BC35/80 and MBC35/80@FH systems, the TPhP degradation was inhibited in BC35 and MBC35@FH systems, and the degradation efficiency reduced from 90 % to 69.09 % and 82.29 %, the k_{obs} decreased from 0.00456 to 0.00237 and 0.00371 within 8 h (Fig. 3e and g), respectively. In contrast, in BC80 and MBC80@FH systems, the TPhP degradation was promoted with the degradation efficiency increased from 90 % to 100 %, and the k_{obs} increased from 0.00456 to 0.00725 and 0.00723 (Fig. 3f and h). Furthermore, in MBC80@FH&PDS system, the degradation efficiency reached 100 % within 6 h which was higher than that of BC80&PDS system. This indicated that the catalytic activity of MBC80@FH is stronger than that of BC80. Therefore, MBC35@FH and MBC80@FH were selected to investigate the main reasons for the difference in catalytic reactions.

$$S_2O_8{}^{2-} \rightarrow 2SO_4\cdot^- \tag{1}$$

$$2SO_4\cdot^- + H_2O \rightarrow SO_4{}^{2-} + \cdot OH + H^+ \tag{2}$$

$$S_2O_8{}^{2-} + 2H_2O \rightarrow 2SO_4{}^{2-} + HO_2{}^- + 3H^+ \tag{3}$$

$$S_2O_8{}^{2-} + HO_2{}^- \rightarrow SO_4{}^{2-} + SO_4\cdot^- + O_2\cdot^- + H^+ \tag{4}$$

$$2O_2\cdot^- + 2H^+ \rightarrow H_2O_2 + {}^1O_2 \tag{5}$$

3.3. The mechanism of PDS activation by catalysts inhibited/enhanced TPhP degradation

The radical trapping experiments revealed that $SO_4\cdot^-$, ·OH, $O_2\cdot^-$ and $^1O_2$ existed in PDS alone system and catalytic systems, and the intensities of various ROS in different reaction systems were as follows: MBC80@FH&PDS > MBC35@FH&PDS > PDS alone (Fig. 4a–c), indicated that both MBC35@FH and MBC80@FH can promote PDS activation to generate more ROS and the activation ability of MBC80@FH is stronger than that of MBC35@FH. The larger SSA, more abundant defect sites and higher Fe content of MBC80@FH than MBC35@FH contributed to its stronger activation of PDS. Theoretically, the more ROS generated, the more TPhP will be degraded. However, in MBC35@FH&PDS system, the phenomenon is the opposite. This may be because MBC35@FH has a strong adsorption ability for TPhP, and adsorbed TPhP on the catalyst quickly diffuses into the catalyst surface and pores, protecting it from ROS attack and becoming an inert component that cannot be oxidized (Georgi and Kopinke, 2005). Pu et al. (2014) found that degradation of diethyl phthalate by PDS reduced through rapid adsorption on activated carbon materials. In addition, the adsorbed TPhP occupied the catalytic active sites on biochar catalyst, a fact that reduced the ability of MBC35@FH to catalyze ROS production from PDS. That may be one reason why the ROS intensity in the MBC35@FH&PDS system is lower than that of MBC80@FH&PDS.

To identify the role of ROS for TPhP degradation in different systems, the radical quenching experiments were conducted. MeOH can quench $SO_4\cdot^-$ (2.5×10^7 $M^{-1}S^{-1}$) and ·OH (9.7×10^8 $M^{-1}S^{-1}$) (Yin et al., 2018) at the same time. TBA can quench ·OH (3.8–7.6×10^8 $M^{-1}S^{-1}$) (Anipsitakis and Dionysiou, 2004), BQ was used to quench $O_2\cdot^-$, and L–histidine was used to quench $^1O_2$ (3.2×10^7 $M^{-1}S^{-1}$) (Ahmadi and

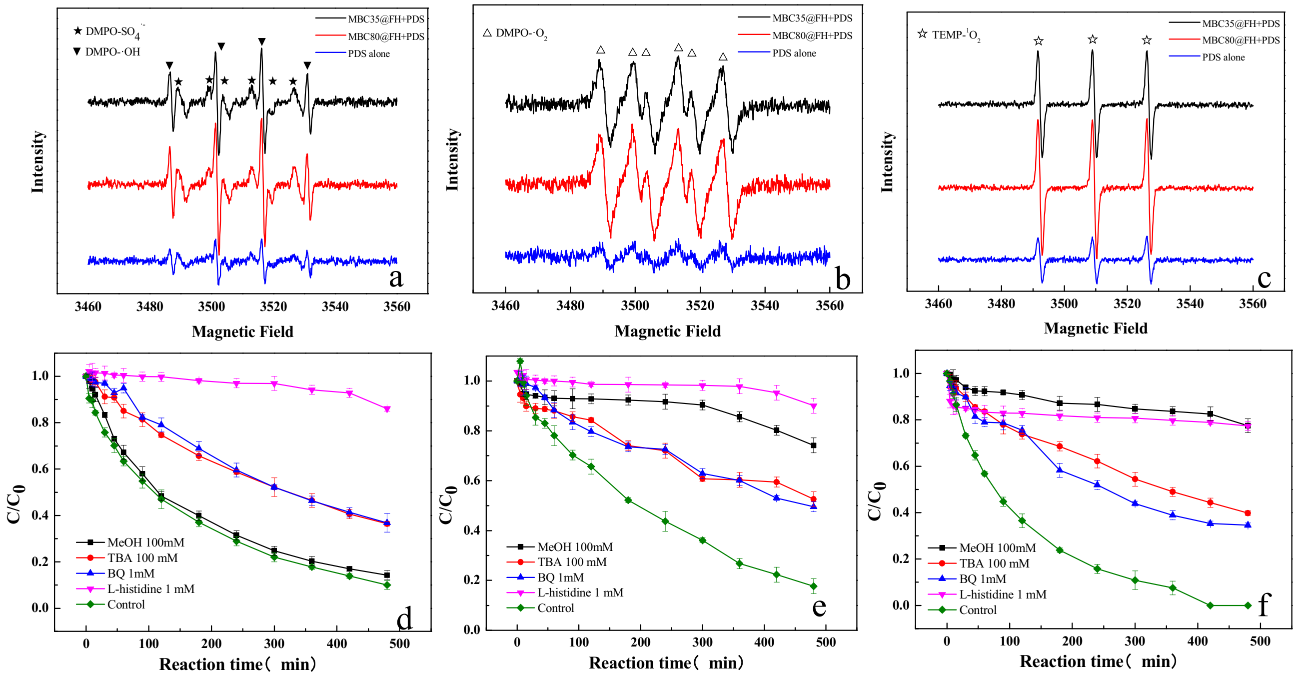

Fig. 4. The EPR spectroscopy of DMPO (a, b) and TEMP (c) trapping; the effect of MeOH, TBA, BQ and L–histidine on TPhP degradation in PDS (d), MBC35@FH&PDS (e) and MBC80@FH&PDS (f) systems. [TPhP] = 10 μM; [catalytic] = 0.1 g/L; [PDS] = 10 mM; [pH] = 6.12; [temperature] = 30 °C.

Ghanbari, 2018). When excessive MeOH was added to the PDS alone system, the degradation efficiency of TPhP was almost unchanged, while the degradation efficiency decreased from 90 % to 63.6 % and 63.2 % with the addition of TBA and BQ (Fig. 4d), indicating that ·OH and $O_2·^-$ played a certain role in oxidative degradation. After the addition of L–histidine, the degradation efficiency of TPhP decreased to 13.98 % (Fig. 4d), suggesting that $^1O_2$ played a crucial role for TPhP degradation in PDS alone system. In MBC80@FH&PDS system, after adding MeOH and TBA, the degradation efficiency of TPhP decreased by 77.47 % and 39.82 % (Fig. 4f), respectively, indicating that $SO_4·^-$ has a stronger degradation effect than ·OH. After adding L–histidine and BQ, the degradation efficiency decreased by 77.31 % and 34.58 % (Fig. 4f), demonstrating that $^1O_2$ and $O_2·^-$ also played a role in degradation. In MBC35@FH&PDS system, after adding MeOH, TBA, L–histidine and BQ, the degradation efficiency decreased by 56.47 %, 34.9 %, 72.39 % and 31.85 %, respectively (Fig. 4e), suggesting that $^1O_2$ and $SO_4·^-$ play a stronger degradation role than ·OH and $O_2·^-$ in this system. All above results indicated that $^1O_2$ and $SO_4·^-$ played a major role in TPhP degradation both in MBC35@FH&PDS and MBC80@FH&PDS systems.

3.4. Activating mechanism of PDS by MBC35/80@FH

XPS analysis showed that Fe, functional groups (oxygen–containing functional groups, pyrrolic nitrogen) and persistent free radicals (PFRs) on the catalysts were involved in the activation of PDS to generate ROS (Figs. 5 and 6d). The peaks of Fe2$p_{3/2}$ at 712.4 eV and 710.2 eV are assigned to Fe^{3+} and Fe^{2+}, respectively (Fu et al., 2019a) (Fig. 5a–d). After the catalytic reaction, Fe^{3+} in MBC80@FH decreased from 52.96 % to 46.82 %, and Fe^{2+} increased from 47.04 % to 53.18 %. A similar phenomenon was observed in MBC35@FH/PDS (Fig. 5a–b). It is suggested that redox transformation between Fe^{3+} and Fe^{2+} occurred during the catalytic reaction. Generally, Fe^{3+} does not directly activate PDS to generate ROS, but Fe^{3+} could react with PDS to generate $S_2O_8·^-$ and Fe^{2+} (Eq. (6)), and then Fe^{2+} donated an electron to PDS. After PDS obtained an electron, the O—O bond was broken and decomposed to generate $SO_4·^-$ and Fe^{3+} (Eqs. (7)–(8)). The produced $SO_4·^-$ reacted with H_2O to form ·OH (Eq. (2)) (Yu et al., 2019). Excess $SO_4·^-$ can also be consumed by self–reaction or reaction with $S_2O_8^{2-}$ (Eqs. (8)–(9)), which may be a reason why $SO_4·^-$ does not play a role in TPhP degradation in the PDS alone system. Meanwhile, during the activation of PDS, the ubiquitous H_2O and O_2 in solution reacted with $S_2O_8^{2-}$ and Fe^{2+} to generate HO_2^-, $SO_4·^-$, and $O_2·^-$ (Eqs. (3)–(4), (10)). The H^+ released continuously during these reactions and then reacted with $O_2·^-$ to form $^1O_2$ (Eq. (5)) (Luo et al., 2022). In addition, oxygen–containing functional groups and pyrrolic nitrogen, as electron–rich groups, can donate electrons to PDS, thereby activating PDS to generate ROS (Tang et al., 2018). According to deconvolution of C1 speaks, the content of C–OH and COOH decreased after catalytic reaction, but new characteristic peaks were formed (Fig. 5e–h). These results indicated that oxygen–containing functional groups participated in the reaction and generated new species (Eqs. (12)–(13)). After the reaction, the pyrrolic nitrogen of MBC35/80@FH decreased by 47.08 % and 33.53 %, respectively (Fig. 5i–l), which may attribute to the consumption during the reaction. PFRs in biochar catalysts can also act as electron donors, activating oxygen in solution to produce $O_2·^-$ (Eq. (11)) (Liu et al., 2020a) (Fig. 6d).

$$Fe^{3+} + S_2O_8{}^{2-} \rightarrow Fe^{2+} + S_2O_8·^- \quad (6)$$

$$Fe^{2+} + S_2O_8{}^{2-} \rightarrow SO_4·^- + Fe^{3+} + SO_4{}^{2-} \quad (7)$$

$$SO_4·^- + SO_4·^- \rightarrow S_2O_8{}^{2-} \quad (8)$$

$$SO_4·^- + S_2O_8{}^{2-} \rightarrow S_2O_8{}^- + SO_4{}^{2-} \quad (9)$$

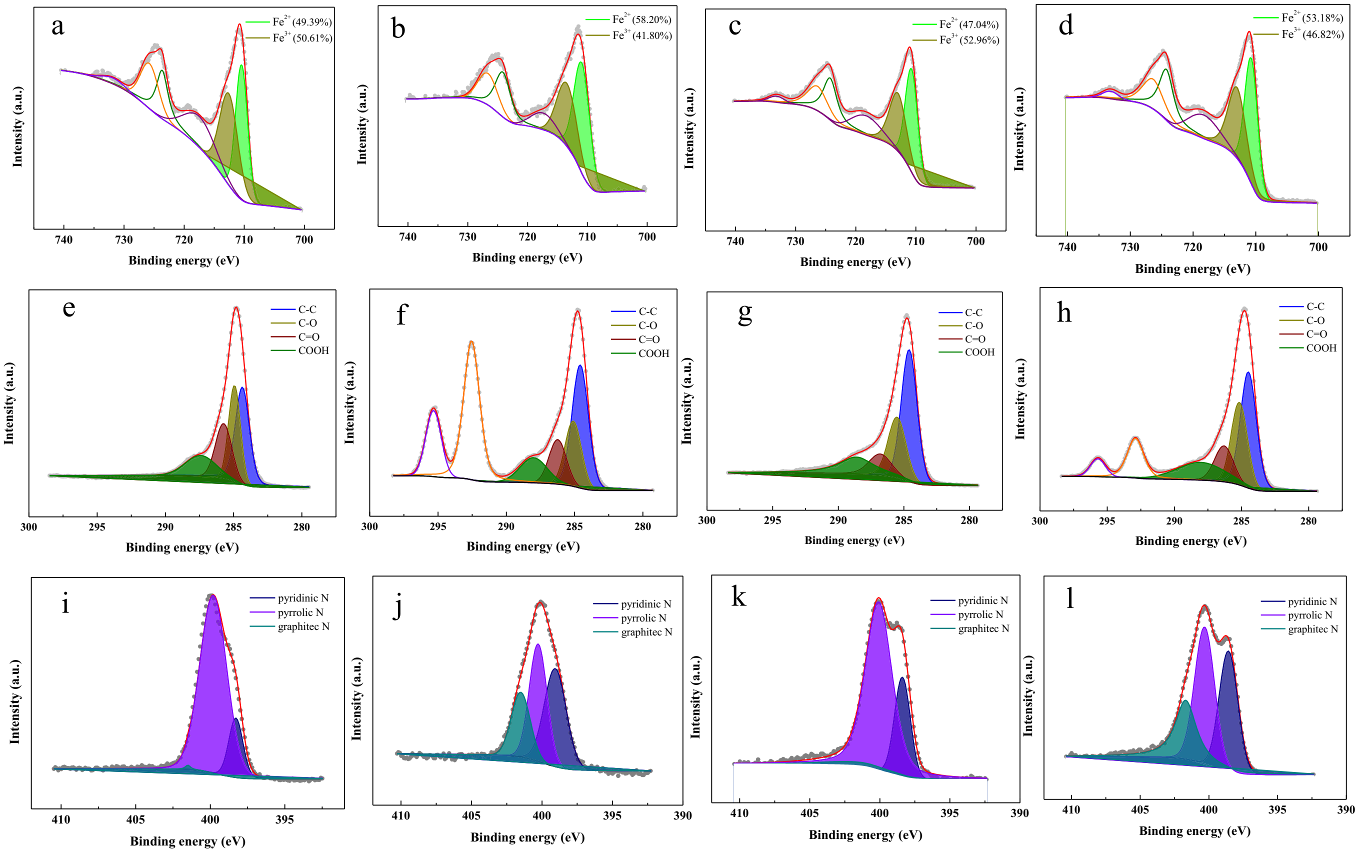

Fig. 5. The deconvolution spectra of Fe2p (a–d), C1s (e–h) and N1s (i–l) before (a, e, i, c, g, k) and after (b, f, j, d, h, l) degradation. MBC35@FH: a, b, e, f, i, j; MBC80@FH: c, d, g, h, k, l.

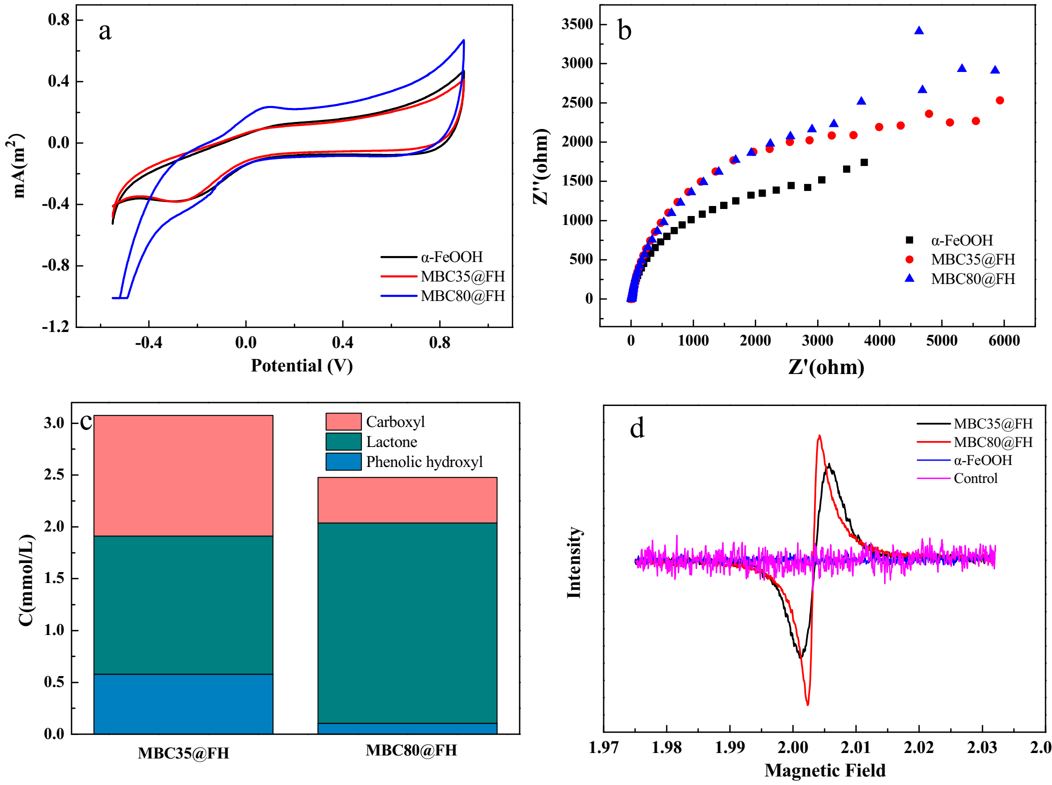

Fig. 6. CV curves (a), EIS Nyquist plots (b), Boehm analysis (c) and EPR signals (d) of MBC35/80@FH.

$$Fe^{2+} + O_2 \rightarrow Fe^{3+} + O_2{\cdot}^- \qquad (10)$$

$$BC\text{–}PFRs + O_2 \rightarrow BC\text{–}PFRs + O_2{\cdot}^- \qquad (11)$$

$$BC_{suface}\text{–}OOH + S_2O_8{}^{2-} \rightarrow SO_4{\cdot}^- + BC_{suface}\text{–}OO{\cdot} + HSO_4{}^- \qquad (12)$$

$$BC_{suface}\text{–}OH + S_2O_8{}^{2-} \rightarrow SO_4{\cdot}^- + BC_{suface}\text{–}O{\cdot} + HSO_4{}^- \qquad (13)$$

The strength of electron transfer ability can reflect the catalytic performance of catalysts to a certain extent. As shown in cyclic voltammetry curves (Fig. 6a), MBC80@FH had a greater capacitance than MBC35@FH, demonstrating its greater power storage capacity. Although MBC80@FH and MBC35@FH obtained similar arc radius in the EIS Nyquist plot (Fig. 6b), the resistance of MBC80@FH was calculated to be 5696 Ω less than that of MBC35@FH (6806 Ω), indicating it is more prone to electron transfer. In addition, the electron transfer ability of carbon materials is related to the unsaturated functional groups (lactone groups) (Luo et al., 2020). Boehm experiments revealed that the lactone group content of MBC80@FH was 1.93 mmol/L, which was significantly higher than that of MBC35@FH (1.33 mmol/L) (Fig. 6c). Furthermore, MBC80@FH had stronger PFRs signals (Fig. 6d) and more defective active sites than MBC35@FH, favoring its excellent PDS activation performance to produce more ROS, which in turn promoted TPhP degradation.

3.5. Proposed degradation pathways of TPhP in MBC80@FH/PDS system

A total of 7 major degradation products were detected by LC–MS/MS with characteristic *m/z* of 250 (P1), 110.5 (P2), 174.5 (P3), 112.1 (P4), 341.0 (P5), 267.0 (P6), and 283.2 (P7) (Fig. S5). The commercially available standard compounds of diphenyl phosphate and catechol have the same characteristic m/z and nearly uniform LC–MS/MS spectra (Fig. S6) with P1 and P2, which verified their occurrences. In addition, the concentration of P1 increased with increase of degradation time (Fig. S7), indicating the degradation of TPhP was not incomplete and degradation products accumulated during the degradation process. Based on the degradation products and degradation mechanism analysis, the following potential degradation pathways were proposed (Fig. 7). Firstly, ROS attacked the phosphorus central bond and phenoxy bond of TPhP to generate phenoxy and P1 through phosphorus–oxygen bond breaking, phenoxy bond breaking and hydroxylation reactions. Phenoxy further reacted with ROS to generate P2 (Song et al., 2019b), and P2 broke the benzene ring under ROS attack to generate P4 (Zhou et al., 2019). P6 and P3 were formed from P1 by hydroxylation reaction and phenoxy bond breaking, respectively. Study also reported that $SO_4{\cdot}^-$ can attack the benzene ring of P1 to generate a cationic radical by electron transfer, which further reacted with water molecules to generate P6 (Fan et al., 2015). In another pathway, TPhP was degraded to P5 by hydroxylation, and P5 transformed to P6 by phenoxy bond breakage. Then, P7 was produced through hydroxylation or electron transfer of $SO_4{\cdot}^-$ on benzene ring from P6 (Song et al., 2019b). Table S1 listed the calculated bond energies of possible bond cleavage sites in TPhP and its degradation intermediates via density functional theory (DFT) (Text S6). For TPhP, the low bond energies occurred at phenoxy bond (c site, E_c = 90.71 Kcal/mol) and phosphorus–oxygen bond (b site, E_b = 94.91 Kcal/mol), indicating these two positions are more likely to be broken to form P1 and phenoxy. The bond energies of phenoxy bond in P1 (d site, E_d = 92.74 Kcal/mol) and P5 (c site, E_c = 90.00 Kcal/mol) are lower than that of other positions, after cleavage, corresponded to forming P3 and P6, respectively. Obviously, the above results predicted based on Gaussian calculations are consistent with experimentally obtained pathways. It can be seen that phosphorus oxygen bond breakage, phenoxy bond breakage and hydroxylation reactions are the main processes of TPhP degradation in the system.

3.6. Effect of anions, cations, and HA on TPhP degradation

The effects of three anions (Cl^-, HCO_3^-, $H_2PO_4^-$), four cations (Na^+, Mg^{2+}, Ca^{2+}, Fe^{3+}) and dissolved organic matter HA on catalytic degradation of TPhP in MBC80@FH&PDS were investigated. As shown in Fig. S8, Cl^- and HCO_3^- inhibited the TPhP degradation, and the degree of inhibition increased with the increase of Cl^- and HCO_3^- concentrations. When

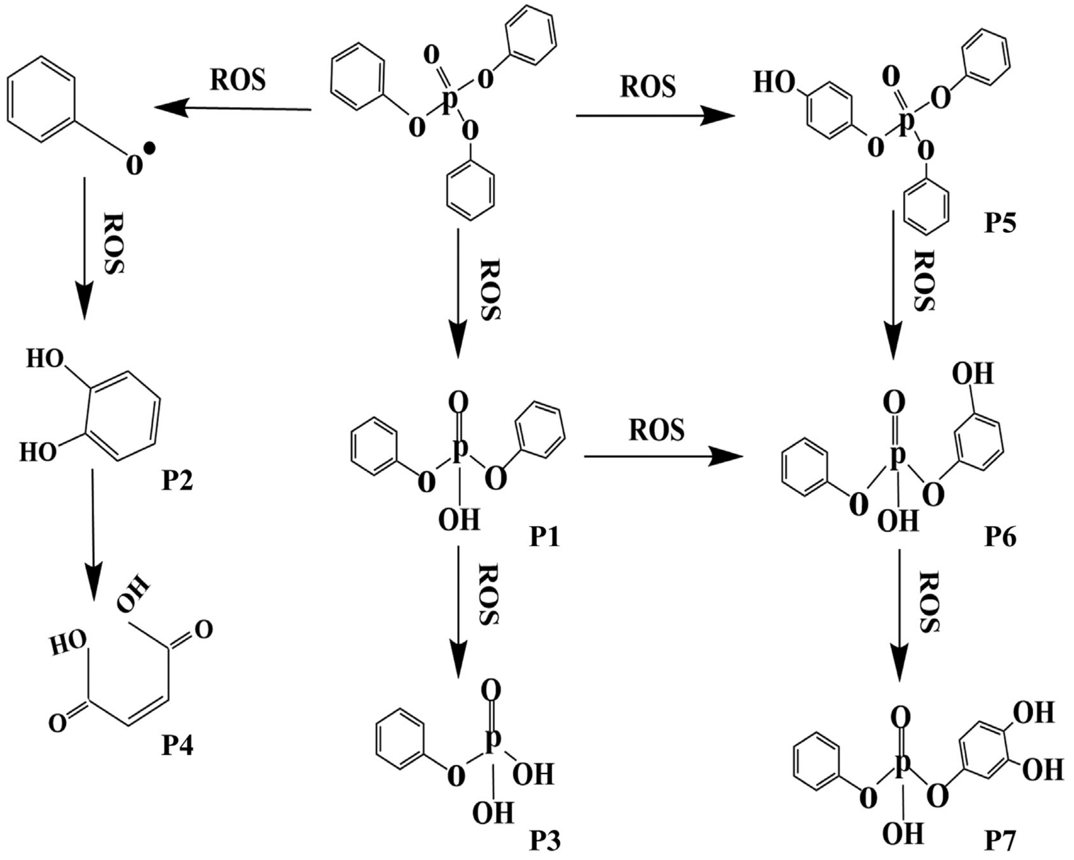

Fig. 7. The schematic graph of degradation pathways of TPhP in MBC80@FH&PDS system.

the concentration of Cl^-/HCO_3^- increased from 0.5 mM to 10 mM, the degradation efficiency of TPhP decreased from 71.64 % to 48.39 %, and from 83.73 % to 66.98 %, respectively (Fig. S8a). Obviously, the inhibition degree of HCO_3^- was lower than that of Cl^-. Both Cl^- and HCO_3^- can react with ROS to consume $SO_4\cdot^-$, $\cdot OH$ and other ROS with strong oxidizing ability, and generated weakly oxidizing $Cl\cdot$, $\cdot Cl_2^-$, $HClO\cdot$ and $HCO_3\cdot$, $CO_3\cdot^-$ (Huang et al., 2021; Wu et al., 2020). The decreased $SO_4\cdot^-$, $\cdot OH$, $^1O_2$ and $O_2\cdot^-$ signals after adding Cl^- during the degradation process (Fig. S9), confirmed the reaction between Cl^- and ROS, thus, resulted in consumption of ROS. Therefore, Cl^- and HCO_3^- inhibited the degradation of TPhP. However, carbonate radicals can react with electron–rich compounds at faster rates (Ji et al., 2015; Song et al., 2019a). The reaction of TPhP as electron–rich compound (Yu et al., 2016) with carbonate radicals attenuated the inhibitory effect of HCO_3^- on degradation. $H_2PO_4^-$ also inhibited the degradation of TPhP by consuming ROS, but the inhibition degree did not change significantly with the concentration of $H_2PO_4^-$ in the range of 0.5–5.0 mM. HA significantly inhibited the TPhP degradation. When the concentration of HA was 0.5, 2.5, 5.0, and 10 mM, the degradation efficiency of TPhP decreased to 83.31 %, 62.86 %, 53.05 % and 41.91 %, respectively (Fig. S8a). The study pointed out that HA is easily adsorbed on the catalyst surface and competes with TPhP for active sites (Wang et al., 2012). Furthermore, it can inhibit degradation by quenching ROS (Liu et al., 2020b).

The effect of Fe^{3+} on TPhP degradation varied with concentration. At low concentrations (0.5–2.5 mM), Fe^{3+} promoted TPhP degradation, while at high concentrations (5.0–10 mM), Fe^{3+} inhibited the degradation (Fig. S8b and S8c). As a representative transition metal, the transformation between Fe^{3+} and Fe^{2+} can activate PDS to generate $SO_4\cdot^-$ and promoted the TPhP degradation, but with increasing concentrations, excessive Fe adsorbed on the catalyst surface, occupied the active sites and excessive Fe^{2+} reacted with $SO_4\cdot^-$ to produce non–oxidizing SO_4^{2-}, which both inhibited degradation. Different from Fe^{3+}, Na^+, Ca^{2+} and Mg^{2+} are in a stable oxidation state and cannot react directly with PDS to form ROS, which theoretically does not affect TPhP degradation. However, the experiments showed that Na^+, Ca^{2+}, and Mg^{2+} significantly inhibited TPhP degradation, and the inhibition degree increased with the increase of cation concentration (Fig. S8b). The zeta potential of MBC80@FH was −19.9 mV, indicating that Na^+, Ca^{2+}, and Mg^{2+} may be adsorbed on MBC80@FH via electrostatic attraction and occupied active sites, therefore, reducing TPhP degradation.

3.7. Recyclability and security of MBC80@FH

The reusability and toxicity of MBC80@FH are related to its practical application, which should be evaluated. After every run, MBC80@FH was collected from reaction solution by filtration, and then washed with methanol and deionized water for three times, respectively. Considering the mass loss during the separation and wash process, 8 parallel experiments were conducted for each cycle to ensure that recovered catalyst was sufficient for next cycle. After three cycles, the degradation efficiency was still reached 100 % within 6 h (Fig. S10), indicating that MBC80@FH had an excellent catalytic stability. When it was used in a real sewage treatment plant influent (11.04 μg/L of TPhP), although the degradation efficiency decreased, it still reached 98.83 % (Fig. S11), showing a good engineering application effect. After reaction, the Fe content of catalyst decreased from 401.03 μg/mg to 207.64 μg/mg, indicated the leaching of iron ions during degradation process. Thus, the leaching concentration of Fe^{2+} (< 84.30 μg/L) and Fe^{3+} (< 64.22 μg/L) were measured in MBC35@FH/MBC80@FH&PDS systems during the TPhP degradation (Fig. S12), the results showed that leaching of total iron was below the European standard (2 ppm). In toxicity assessment experiments, wild–type zebrafish embryos were exposed in 0.1 g/L MBC80@FH solution for 5 days, the hatching rate, malformation rate and mortality rate were 88.33 %, 1.00 % and 1.90 %, respectively, which were not significant different from that of blank control (89. 33 %, 1.51 % and 1.88 %) (Fig. S13), indicating the MBC80@FH was no–toxic to aquatic organisms in this case. The above results suggested that MBC80@FH can be recycled during usage and will not cause secondary pollution to the water body.

4. Conclusion

In summary, TPhP can be degraded in PDS alone system, and the degradation efficiency increased with the increase of reaction temperature and PDS concentration. Both MBC35@FH and MBC80@FH could activate PDS to produce more ROS and the intensities of various ROS in different reaction systems were as follows: MBC80@FH&PDS > MBC35@FH&PDS > PDS alone. However, the degradation of TPhP was inhibited by MBC35@FH, while MBC80@FH promoted TPhP degradation. The influence of MBC@FH on PDS activation was correlated to their physicochemical properties. The larger SSA, more abundant defect sites, higher Fe content, more PFRs and stronger electron transfer capability of MBC80@FH than MBC35@FH contributed to its stronger PDS activation for TPhP degradation. The degradation of TPhP mainly involved phosphorus oxygen bond breakage, phenoxy bond breakage and hydroxylation reactions processes. This study might provide a new perspective on the catalyzed degradation of organic contaminants by metallic carbon catalyst.

CRediT authorship contribution statement

Yunjiang Yu: Conceptualization, Methodology, Writing – original draft. **Zijuan Zhong:** Investigation, Data curation. **Haobo Guo:** Investigation, Formal analysis. **Yingxin Yu:** Validation. **Tong Zheng:** Data curation. **Hongyan Li:** Supervision. **Zhaofeng Chang:** Investigation, Formal analysis, Software, Supervision, Writing – review & editing.

Data availability

Data will be made available on request.

Declaration of competing interest

The authors declare that they have no known competing financial interests or personal relationships that could have appeared to influence the work reported in this paper.

Acknowledgments

This work was supported by National Natural Science Foundation of China (42107266), National Key Research and Development Program of China (2019YFC1803403, 2021YFC1808901 and 2021YFC1808902).

Appendix A. Supplementary data

Supplementary data to this article can be found online at https://doi.org/10.1016/j.scitotenv.2022.159940.

References

Ahmadi, M., Ghanbari, F., 2018. Degradation of organic pollutants by photoelectro–peroxone/ZVI process: synergistic, kinetic and feasibility studies. J. Environ. Manag. 228, 32–39. https://doi.org/10.1016/j.jenvman.2018.08.102.

Anipsitakis, G.P., Dionysiou, D.D., 2004. Radical generation by the interaction of transition metals with common oxidants. Environ. Sci. Technol. 38 (13), 3705–3712. https://doi.org/10.1021/es035121o.

Blum, A., Behl, M., Birnbaum, L.S., Diamond, M.L., Phillips, A., Singla, V., Sipes, N.S., Stapleton, H.M., Venier, M., 2019. Organophosphate Ester flame retardants: are they a regrettable substitution for polybrominated diphenyl ethers? Environ. Sci. Technol. Lett. 6 (11), 638–649. https://doi.org/10.1021/acs.estlett.9b00582.

Boehm, H.P., 1994. Some aspects of the surface–chemistry of carbon–blacks and other carbons. Carbon 32 (5), 759–769. https://doi.org/10.1016/0008-6223(94)90031-0.

Canbaz, D., Logiantara, A., Van Ree, R., van Rijt, L.S., 2017. Immunotoxicity of organophosphate flame retardants TPHP and TDCIPP on murine dendritic cells in vitro. Chemosphere 177, 56–64. https://doi.org/10.1016/j.chemosphere.2017.02.149.

Cequier, E., Ionas, A.C., Covaci, A., Maria Marce, R., Becher, G., Thomsen, C., 2014. Occurrence of a broad range of legacy and emerging flame retardants in indoor environments in Norway. Environ. Sci. Technol. 48 (12), 6827–6835. https://doi.org/10.1021/es500516u.

Dai, Y., Zhang, N., Xing, C., Cui, Q., Sun, Q., 2019. The adsorption, regeneration and engineering applications of biochar for removal organic pollutants: a review. Chemosphere 223, 12–27. https://doi.org/10.1016/j.chemosphere.2019.01.161.

Fan, Y., Ji, Y., Kong, D., Lu, J., Zhou, Q., 2015. Kinetic and mechanistic investigations of the degradation of sulfamethazine in heat–activated persulfate oxidation process. J. Hazard. Mater. 300, 39–47. https://doi.org/10.1016/j.jhazmat.2015.06.058.

Fang, G.D., Dionysiou, D.D., Zhou, D.M., Wang, Y., Zhu, X.D., Fan, J.X., Gang, L., Wang, Y.J., 2013. Transformation of polychlorinated biphenyls by persulfate at ambient temperature. Chemosphere 90 (5), 1573–1580. https://doi.org/10.1016/j.chemosphere.2012.07.047.

Fu, H., Ma, S., Zhao, P., Xu, S., Zhan, S., 2019a. Activation of peroxymonosulfate by graphitized hierarchical porous biochar and MnFe2O4 magnetic nanoarchitecture for organic pollutants degradation: structure dependence and mechanism. Chem. Eng. J. 360, 157–170. https://doi.org/10.1016/j.cej.2018.11.207.

Fu, H., Zhao, P., Xu, S., Cheng, G., Li, Z., Li, Y., Li, K., Ma, S., 2019b. Fabrication of Fe3O4 and graphitized porous biochar composites for activating peroxymonosulfate to degrade p–hydroxybenzoic acid: insights on the mechanism. Chem. Eng. J. 375. https://doi.org/10.1016/j.cej.2019.121980.

Ge, X., Ma, Y., Song, X., Wang, G., Zhang, H., Zhang, Y., Zhao, H., 2017. beta–FeOOH Nanorods/Carbon foam-based hierarchically porous monolith for highly effective arsenic removal. ACS Appl. Mater. Interfaces 9 (15), 13480–13490. https://doi.org/10.1021/acsami.7b01275.

Georgi, A., Kopinke, F.D., 2005. Interaction of adsorption and catalytic reactions in water decontamination processes part I. Oxidation of organic contaminants with hydrogen peroxide catalyzed by activated carbon. Appl. Catal. B. 58 (1–2), 9–18. https://doi.org/10.1016/j.apcatb.2004.11.014.

Guo, M., Song, W., Tian, J., 2020. Biochar-facilitated soil remediation: mechanisms and efficacy variations. Front. Environ. Sci. 8. https://doi.org/10.3389/fenvs.2020.521512.

House, D.A., 1962. Kinetics and mechanism of oxidations by peroxydisulfate. Chem. Rev. 62 (3). https://doi.org/10.1021/cr60217a001 185-000.

Hu, W., Gao, F., Zhang, H., Hiromori, Y., Arakawa, S., Nagase, H., et al., 2017. Activation of peroxisome proliferator-activated receptor gamma and disruption of progesterone synthesis of 2–Ethylhexyl diphenyl phosphate in human placental choriocarcinoma cells: comparison with triphenyl phosphate. Environ. Sci. Technol. 51 (7), 4061–4068. https://doi.org/10.1021/acs.est.7b00872.

Huang, H., Guo, T., Wang, K., Li, Y., Zhang, G., 2021. Efficient activation of persulfate by a magnetic recyclable rape straw biochar catalyst for the degradation of tetracycline hydrochloride in water. Sci. Total Environ. 758. https://doi.org/10.1016/j.scitotenv.2020.143957.

Ji, Y., Fan, Y., Liu, K., Kong, D., Lu, J., 2015. Thermo activated persulfate oxidation of antibiotic sulfamethoxazole and structurally related compounds. Water Res. 87, 1–9. https://doi.org/10.1016/j.watres.2015.09.005.

Kim, J.W., Isobe, T., Muto, M., Nguyen Minh, T., Katsura, K., Malarvannan, G., Sudaryanto, A., Chang, K.H., Prudente, M., Pham Hung, V., Takahashi, S., Tanabe, S., 2014. Organophosphorus flame retardants (PFRs) in human breast milk from several asian countries. Chemosphere 116, 91–97. https://doi.org/10.1016/j.chemosphere.2014.02.033.

Kong, Z., Lu, L., Zhu, C., Xu, J.J., Fang, Q., Liu, R.L., Shen, Y., 2022. Enhanced adsorption and photocatalytic removal of PFOA from water by F–functionalized MOF with in–situ–growth TiO2: regulation of electron density and bandgap. Sep. Purif. Technol. 297. https://doi.org/10.1016/j.seppur.2022.121449.

Lin, Y., Wu, S., Yang, C., Chen, M., Li, X., 2019. Preparation of size–controlled silver phosphate catalysts and their enhanced photocatalysis performance via synergetic effect with MWCNTs and PANI. Appl. Catal. B. 245, 71–86. https://doi.org/10.1016/j.apcatb.2018.12.048.

Liu, Z., Zhang, L., Sheng, L., Zhou, Q., Wei, T., Feng, J., Fan, Z., 2018. Edge-nitrogen-rich carbon dots pillared graphene blocks with ultrahigh Volumetric/Gravimetric capacities and ultralong life for sodium-ion storage. Adv. Energy Mater. 8 (30). https://doi.org/10.1002/aenm.201802042.

Liu, B., Guo, W., Wang, H., Si, Q., Zhao, Q., Luo, H., Ren, N., 2020a. Activation of peroxymonosulfate by cobalt–impregnated biochar for atrazine degradation: the pivotal roles of persistent free radicals and ecotoxicity assessment. J. Hazard. Mater. 398. https://doi.org/10.1016/j.jhazmat.2020.122768.

Liu, L., Xu, X., Li, Y., Su, R., Li, Q., Zhou, W., Gao, B., Yue, Q., 2020b. One–step synthesis of "nuclear–shell" structure iron–carbon nanocomposite as a persulfate activator for bisphenol a degradation. Chem. Eng. J. 382. https://doi.org/10.1016/j.cej.2019.122780.

Lu, L., Yu, W.T., Wang, Y.F., Zhang, K., Zhu, X.M., Zhang, Y.C., Wu, Y.J., Ullah, H., Xiao, X., Chen, B., 2020. Application of biochar-based materials in environmental remediation: from multi–level structures to specific devices. Biochar 2, 1–31. https://doi.org/10.1007/s42773-020-00041-7.

Luo, H., Lin, Q., Zhang, X., Huang, Z., Fu, H., Xiao, R., Liu, S.S., 2020. Determining the key factors of nonradical pathway in activation of persulfate by metal–biochar nanocomposites for bisphenol a degradation. Chem. Eng. J. 391. https://doi.org/10.1016/j.cej.2019.123555.

Luo, J., Yi, Y., Ying, G., Fang, Z., Zhang, Y., 2022. Activation of persulfate for highly efficient degradation of metronidazole using Fe(II)–rich potassium doped magnetic biochar. Sci. Total Environ. 819. https://doi.org/10.1016/j.scitotenv.2021.152089.

Matsukami, H., Nguyen Minh, T., Suzuki, G., Someya, M., Le Huu, T., Pham Hung, V., Takahashi, S., Tanabe, S., Takigami, H., 2015. Flame retardant emission from e-waste recycling operation in northern Vietnam: environmental occurrence of emerging organophosphorus esters used as alternatives for PBDEs. Sci. Total Environ. 514, 492–499. https://doi.org/10.1016/j.scitotenv.2015.02.008.

Ouyang, D., Chen, Y., Yan, J., Qian, L., Han, L., Chen, M., 2019. Activation mechanism of peroxymonosulfate by biochar for catalytic degradation of 1,4–dioxane: important role of biochar defect structures. Chem. Eng. J. 370, 614–624. https://doi.org/10.1016/j.cej.2019.03.235.

Pu, M., Ma, Y., Wan, J., Wang, Y., Huang, M., Chen, Y., 2014. Fe/S doped granular activated carbon as a highly active heterogeneous persulfate catalyst toward the degradation of Orange G and diethyl phthalate. J. Colloid Interface Sci. 418, 330–337. https://doi.org/10.1016/j.jcis.2013.12.034.

Shan, D., Deng, S., Zhao, T., Wang, B., Wang, Y., Huang, J., Yu, G., Winglee, J., Wiesner, M.R., 2016. Preparation of ultrafine magnetic biochar and activated carbon for pharmaceutical adsorption and subsequent degradation by ball milling. J. Hazard. Mater. 305, 156–163. https://doi.org/10.1016/j.jhazmat.2015.11.047.

Shi, M., Wang, X., Shao, M.Y., Lu, L., Ullah, H., Zheng, H., Li, F.M., 2022. Resource utilization of typical biomass wastes as biochars in removing plasticizer diethyl phthalate from water: characterization and adsorption mechanisms. Front. Environ. Sci. Eng. 17, 5. https://doi.org/10.1007/s11783-023-1605-4.

Smith, M., Scudiero, L., Espinal, J., McEwen, J.S., Garcia-Perez, M., 2016. Improving the deconvolution and interpretation of XPS spectra from chars by ab initio calculations. Carbon 110, 155–171. https://doi.org/10.1016/j.carbon.2016.09.012.

Song, H., Yan, L., Ma, J., Jiang, J., Cai, G., Zhang, W., Zhang, Z., Zhang, J., Yang, T., 2017. Nonradical oxidation from electrochemical activation of peroxydisulfate at Ti/Pt anode: efficiency, mechanism and influencing factors. Water Res. 116, 182–193. https://doi.org/10.1016/j.watres.2017.03.035.

Song, Q., Feng, Y., Liu, G., Lv, W., 2019a. Degradation of the flame retardant triphenyl phosphate by ferrous ion–activated hydrogen peroxide and persulfate: kinetics, pathways, and mechanisms. Chem. Eng. J. 361, 929–936. https://doi.org/10.1016/j.cej.2018.12.140.

Song, Q., Feng, Y., Wang, Z., Liu, G., Lv, W., 2019b. Degradation of triphenyl phosphate (TPhP) by CoFe2O4–activated peroxymonosulfate oxidation process: kinetics, pathways, and mechanisms. Sci. Total Environ. 681, 331–338. https://doi.org/10.1016/j.scitotenv.2019.05.105.

Tang, L., Liu, Y., Wang, J., Zeng, G., Deng, Y., Dong, H., Feng, H., Wang, J., Peng, B., 2018. Enhanced activation process of persulfate by mesoporous carbon for degradation of aqueous organic pollutants: electron transfer mechanism. Appl. Catal. B. 231, 1–10. https://doi.org/10.1016/j.apcatb.2018.02.059.

Van der Veen, I., de Boer, J., 2012. Phosphorus flame retardants: properties, production, environmental occurrence, toxicity and analysis. Chemosphere 88 (10), 1119–1153. https://doi.org/10.1016/j.chemosphere.2012.03.067.

Wang, J., Wang, S., 2019. Preparation, modification and environmental application of biochar: a review. J. Clean. Prod. 227, 1002–1022. https://doi.org/10.1016/j.jclepro.2019.04.282.

Wang, C., Zhu, L., Wei, M., Chen, P., Shan, G., 2012. Photolytic reaction mechanism and impacts of coexisting substances on photodegradation of bisphenol a by Bi2WO6 in water. Water Res. 46 (3), 845–853. https://doi.org/10.1016/j.watres.2011.11.057.

Wang, W., Deng, S., Ren, L., Li, D., Wang, W., Vakili, M., Wang, B., Huang, J., Wang, Y., Yu, G., 2018. Stable covalent organic frameworks as efficient adsorbents for high and selective removal of an aryl-organophosphorus flame retardant from water. ACS Appl. Mater. Interfaces 10 (36), 30265–30272. https://doi.org/10.1021/acsami.8b06229.

Wu, X., Zhao, W., Huang, Y., Zhang, G., 2020. A mechanistic study of amorphous CoSx cages as advanced oxidation catalysts for excellent peroxymonosulfate activation towards antibiotics degradation. Chem. Eng. J. 381. https://doi.org/10.1016/j.cej.2019.122768.

Wu, L., Zhao, X., Bi, E., 2022. Predicting the effect of dissolved humic acid on sorption of benzotriazole to biochar. Biochar 4 (1). https://doi.org/10.1007/s42773-022-00134-5.

Yang, Y., Lu, X., Jiang, J., Ma, J., Liu, G., Cao, Y., Liu, W., Li, J., Pang, S., Kong, X., Luo, C., 2017. Degradation of sulfamethoxazole by UV, UV/H2O2 and UV/persulfate (PDS): formation of oxidation products and effect of bicarbonate. Water Res. 118, 196–207. https://doi.org/10.1016/j.watres.2017.03.054.

Yang, F., Zhang, S., Li, H., Li, S., Cheng, K., Li, J.S., Tsang, D.C.W., 2018. Corn straw–derived biochar impregnated with alpha–FeOOH nanorods for highly effective copper removal. Chem. Eng. J. 348, 191–201. https://doi.org/10.1016/j.cej.2018.04.161.

Yin, R., Guo, W., Wang, H., Du, J., Zhou, X., Wu, Q., Zheng, H., Chang, J., Ren, N., 2018. Selective degradation of sulfonamide antibiotics by peroxymonosulfate alone: direct oxidation and nonradical mechanisms. Chem. Eng. J. 334, 2539–2546. https://doi.org/10.1016/j.cej.2017.11.174.

Yu, Q., Xie, H.B., Chen, J., 2016. Atmospheric chemical reactions of alternatives of polybrominated diphenyl ethers initiated by center dot OH: a case study on triphenyl phosphate. Sci. Total Environ. 571, 1105–1114. https://doi.org/10.1016/j.scitotenv.2016.07.105.

Yu, J., Tang, L., Pang, Y., Zeng, G., Wang, J., Deng, Y., Liu, Y., Feng, H., Chen, S., Ren, X., 2019. Magnetic nitrogen–doped sludge–derived biochar catalysts for persulfate activation: internal electron transfer mechanism. Chem. Eng. J. 364, 146–159. https://doi.org/10.1016/j.cej.2019.01.163.

Yu, Y., Guo, H., Zhong, Z., Wang, A., Xiang, M., Xu, S., Dong, C., Chang, Z., 2022. Fe3O4 loaded on ball milling biochar enhanced bisphenol a removal by activating persulfate: performance and activating mechanism. J. Environ. Manag. 319. https://doi.org/10.1016/j.jenvman.2022.115661.

Zeng, X., He, L., Cao, S., Ma, S., Yu, Z., Gui, H., Sheng, G., Fu, J., 2014. Occurrence and distribution of organophosphate flame retardants/plasticizers in wastewater treatment plant sludges from the pearl river delta, China. Environ. Toxicol. Chem. 33 (8), 1720–1725. https://doi.org/10.1002/etc.2604.

Zhang, Y., Su, H., Ya, M., Li, J., Ho, S.H., Zhao, L., Jian, K., Letcher, R.J., Su, G., 2019. Distribution of flame retardants in smartphones and identification of current–use organic chemicals including three novel aryl organophosphate esters. Sci. Total Environ. 693. https://doi.org/10.1016/j.scitotenv.2019.133654.

Zhang, S., Du, Q., Sun, Y., Song, J., Yang, F., Tsang, D.C.W., 2020. Fabrication of L–cysteine stabilized alpha–FeOOH nanocomposite on porous hydrophilic biochar as an effective adsorbent for Pb2+ removal. Sci. Total Environ. 720. https://doi.org/10.1016/j.scitotenv.2020.137415.

Zhang, X., Gang, D.D., Sun, P., Lian, Q., Yao, H., 2021. Goethite dispersed corn straw–derived biochar for phosphate recovery from synthetic urine and its potential as a slow–release fertilizer. Chemosphere 262. https://doi.org/10.1016/j.chemosphere.2020.127861.

Zhao, F., Kang, Q., Zhang, X., Liu, J., Hu, J., 2019. Urinary biomarkers for assessment of human exposure to monomeric aryl phosphate flame retardants. Environ. Int. 124, 259–264. https://doi.org/10.1016/j.envint.2019.01.022.

Zhao, L., Zhang, H., Zhao, B., Lyu, H., 2022. Activation of peroxydisulfate by ball–milled alpha–FeOOH/biochar composite for phenol removal: component contribution and internal mechanisms. Environ. Pollut. 293. https://doi.org/10.1016/j.envpol.2021.118596.

Zheng, Y., Wan, Y., Chen, J., Chen, H., Gao, B., 2020. MgO modified biochar produced through ball milling: a dual–functional adsorbent for removal of different contaminants. Chemosphere 243. https://doi.org/10.1016/j.chemosphere.2019.125344.

Zhou, P., Zhang, J., Zhang, G., Li, W., Liu, Y., Cheng, X., Huo, X., Liu, Y., Zhang, Y., 2019. Degradation of dimethyl phthalate by activating peroxymonosulfate using nanoscale zero valent tungsten: mechanism and degradation pathway. Chem. Eng. J. 359, 138–148. https://doi.org/10.1016/j.cej.2018.11.123.

Zhou, Y., Li, Z., Zhu, Y., Chang, Z., Hu, Y., Tao, L., Zheng, T., Xiang, M., Yu, Y., 2022. Legacy and alternative flame retardants in indoor dust from e–waste industrial parks and adjacent residential houses in South China: variations, sources, and health implications. Sci. Total Environ. 845. https://doi.org/10.1016/j.scitotenv.2022.157307.

Zhu, K., Wang, X., Geng, M., Chen, D., Lin, H., Zhang, H., 2019. Catalytic oxidation of clofibric acid by peroxydisulfate activated with wood–based biochar: effect of biochar pyrolysis temperature, performance and mechanism. Chem. Eng. J. 374, 1253–1263. https://doi.org/10.1016/j.cej.2019.06.006.

Zhu, C., Lu, L., Xu, J.J., Song, S., Fang, Q., Liu, R.L., Shen, Y.X., Zhao, J.K., Dong, W., Shen, Y., 2023. Metal monovacancy-induced spin polarization for simultaneous energy recovery and wastewater purification. Chem. Eng. J. 451. https://doi.org/10.1016/j.cej.2022.138537.